

## Thermal error modeling of spindle and dynamic machining accuracy reliability analysis of CNC machine tools based on IA and LHSMC

Indexed by:



Ziling Zhang<sup>a\*</sup>, Shuo Feng<sup>a</sup>, Yan Ding<sup>b</sup>, Xiao Mei<sup>a</sup>, Zhiqiang Tao<sup>c</sup>

<sup>a</sup>Shanghai Maritime University, Logistics Engineering College, Shanghai, 201306, China

<sup>b</sup>Qiqihar Second Machine Tool (Group) Co.Ltd., Heilongjiang, 161005, China

<sup>c</sup>Beijing Union University, College of Robotics, Beijing, 100027, China


### Highlights

- A thermal error model of spindle unit is developed based on IA.
- A machining accuracy model considering the thermal error is constructed based on MBS.
- The machining accuracy reliability analysis method is presented based on LHSMC.
- The effectiveness of the method is verified by a four-axis machine tool.

### Abstract

Machining accuracy reliability as a key index of CNC machine tools is seriously influenced by the geometric and thermal errors. In the paper, a spindle unit thermal error modeling and machining accuracy reliability analysis method is proposed. By analyzing the heat generation mechanism, a thermal error model was developed to describe the thermal deformation of the electric spindle. Based on the immune algorithm (IA), the heat generation power and the heat transfer coefficient were optimized, and the thermal error was obtained by finite element thermal-mechanical coupling. By adopting the multi-body system theory (MBS), a dynamic machining accuracy model was put forward including the geometric and thermal errors. Based on the Latin hypercube sampling Monte Carlo method (LHSMC), a machining accuracy reliability analysis method was proposed to characterize the machining accuracy reliability considering the geometric and thermal errors. The method was employed to a machine tool, and the experimental results indicate the verification and superiority of the method.

### Keywords

This is an open access article under the CC BY license (<https://creativecommons.org/licenses/by/4.0/>) 

electric spindle unit, thermal error, latin hypercube sampling monte carlo method, finite element simulation, machining accuracy reliability.

## 1. Introduction

CNC machine tools are favored by various enterprises as core equipment owing to their high-speed and high-accuracy characteristics. Machining accuracy reliability is an important criterion, which reflects the capability of machine tools to achieve the desired requirements. The machining accuracy is directly expressed in the dimensional error of the workpiece in the work condition. Geometric and thermal errors are the major contributors to variations in machining accuracy [21, 23]. Among the total error sources, the occupancy rate of thermal error is 40%-75% [14]. The higher machining accuracy reliability of machine tools, the greater their competitiveness, which is a factor that manufacturers need to focus on [4]. Thus, it is crucial to consider the impact of thermal error on the machining accuracy reliability. With the increased requirements for high precision and efficiency in manufacturing technology, the effective prediction of thermal error is becoming increasingly important in studying machining accuracy [30]. Hence, how to characterize the reliability of machining

accuracy under the effect of thermal error is critical to evaluate the machining capability of machine tools [18].

The temperature variation of the motor and bearings are the major cause of thermal error [15]. Since it is difficult to be calculated effectively, scientific modeling methods to predict the thermal error are necessary [13]. The thermal error modeling process has the following steps: analyzing the spindle temperature rise field; establishing the connection between the critical region of temperature and thermal deformation field; collecting the critical region temperature to predict the thermal error [24]. Recently, many scholars have devoted themselves to the research of thermal error modeling methods. Zhao et al. calculated the convection heat transfer coefficient on the spindle surface, the temperature and deformation fields of the spindle were derived based on the finite element method and validated experimentally [31]. Hou et al. analyzed the coupled thermal deformation of machine tool components, and a multi-objective genetic algorithm was applied to derive a high robustness thermal error model [6]. By using the improved particle swarm optimization (IPSO) method, Li et al. developed a thermal error model, and the higher modeling efficiency

(\* ) Corresponding author.

E-mail addresses: Ziling Zhang: [zhangziling1119@126.com](mailto:zhangziling1119@126.com), Shuo Feng: [fengshuojxq@163.com](mailto:fengshuojxq@163.com), Yan Ding: [ding-4560@163.com](mailto:ding-4560@163.com), Xiao Mei: [xiaomei@shmtu.edu.cn](mailto:xiaomei@shmtu.edu.cn), Zhiqiang Tao: [jqrzhiqiang@buu.edu.cn](mailto:jqrzhiqiang@buu.edu.cn)

and accuracy were validated by experiments [11]. Shi et al. introduced a thermal error model by Bayesian neural network, and used fuzzy c-means (FCM) clustering analysis to select the sensitive points of temperature. The model has higher prediction accuracy compared to BP neural network [20]. Uhlmann and Hu established a three-dimensional finite element model to predict the thermal characteristics of electric spindles, quantified the heat transfer process internal to the spindle, and validated it under consideration of complex boundary conditions [22]. Zheng and Chen studied the thermal performance of angular contact bearings, analyzed the heat transfer process of the bearing sub source, and developed a comprehensive thermal grid model to predict the temperature rise of the bearings considering the effect of various factors such as constraints and assembly relationships [33]. To effectively forecast the transient temperature and thermal deformation fields of the spindle unit, Yang et al. developed a coupled thermal-structural model, and compared with the TCP thermal errors obtained by the regression model to validate the feasibility of this model [25].

Most of the above-mentioned thermal error modeling methods were proposed based on empirical formulas, which deviate from the actual situation and decrease predictive performance. In addition, the traditional temperature-thermal error and multivariate-thermal error models did not study the formation mechanism of thermal error of the spindle unit in depth, which leaves room for improvement in the application of these two methods [16]. Hence, how to construct a spindle thermal error model with higher prediction accuracy is an urgent problem.

Meanwhile, geometric and thermal errors are the direct cause of the machining accuracy deviation from the desired requirements [5]. Thus, it is imperative to perform machining accuracy modeling. To this end, there are a lot of efforts made by many researchers to develop modeling methods, such as HTM [10, 7, 26, 5], screw theory [32, 17], D-H method [9], Lagrange method [19], Spearman rank correlation method [3] and so on. Geometric errors can be measured using instruments, the translation geometric errors are determined using a laser interferometer, while the angle errors are determined using a ball-bar [34]. The machining accuracy requires consideration of multiple error sources, which is the key point of this paper's research.

Machining accuracy reliability can effectively indicate the capability of the machine tool to achieve the required machining accuracy [27]. So far, much work has been done by many researchers to characterize the reliability of machines. Cheng et al. developed the reliability and sensitivity model to analyze the machining accuracy of the machine tool based on Monte Carlo method, and verified with a three-axis machine tool [2]. Jiang et al. calculated the reliability of the electric spindle system based on the quasi-Monte Carlo method (QMC), used the Kriging method instead of the QMC method to make the calculation more efficient, and experimentally verified the applicability of the model [8]. Cai et al. developed the machining accuracy reliability and sensitivity models considering multiple failure modes based on the first-order and second-moment (AFOSM) and performed experimental validation [1]. The aforementioned scholars have conducted many works for the reliability of machine tools, which shows that the development of machine tool reliability analysis methods is critical. High accuracy reliability prediction methods can improve the competitiveness of machine tools [12]. Detailed descriptions of this aspect are also provided in this paper.

In the paper, a thermal error modeling of spindle unit and machining accuracy reliability analysis method for CNC machine tools is presented, which has the following advantages:

1. The first advantage is the establishment the thermal error model of the electric spindle based on heat generation mechanism and IA. Besides, the heat generation power and heat transfer coefficient were optimized by IA. This model can reveal the inner mechanism of the thermal error and screen the key factors compared to the current empirical methods and temperature-thermal error neural network methods, which can provide

the methodological support for predicting the spindle thermal error.

2. The second advantage is the development of the machining accuracy model by MBS, which considers the comprehensive influence of geometric and thermal errors. This model extends the prediction of machining accuracy from considering a single error source of geometric errors to a multiple error sources of geometric and thermal errors;
3. The third advantage is the proposal of the machining accuracy reliability analysis method by LHSMC, which considers the multiple error sources and the randomness of errors. What's more, the model expands the machining accuracy reliability assessment from the traditional static category to the dynamic category, which is closer to the actual machining process and can provide a valid theoretical guide to analyze the machining accuracy reliability of machine tools.

The other contents are arranged as follows. Section 2 gives a description of the thermal error modeling and machining accuracy modeling process. In Section 3, the machining accuracy reliability model based on LHSMC is established. Then, a four-axis machine tool is utilized to validate this model through experiments, by comparing with AFOSM in Section 4. The conclusion of the paper is given in section 5.

## 2. Dynamic machining accuracy modeling considering the thermal error of spindle unit

### 2.1. Heat generation mechanism analysis

As the core of the machine tool, the spindle unit contains many heat generating components. Rotating parts such as bearings and motor inevitably generate heat due to the friction under the high speed rotation. When the heat accumulates, the spindle unit generates the deformation. To decrease the large deformation induced by high temperature rise, the spiral cooling water jackets are placed outside the heat generating components to accelerate the heat dissipation process. When the electric spindle unit is working, the existence of temperature gradients internal to the electric spindle unit drives the heat transfer from the high temperature area to the low temperature area. The components in contact with the air transfer heat to the air in the form of thermal radiation. The heat transfer process between the coolant and the heat generating components carries away most of the heat, as shown in Fig. 1.

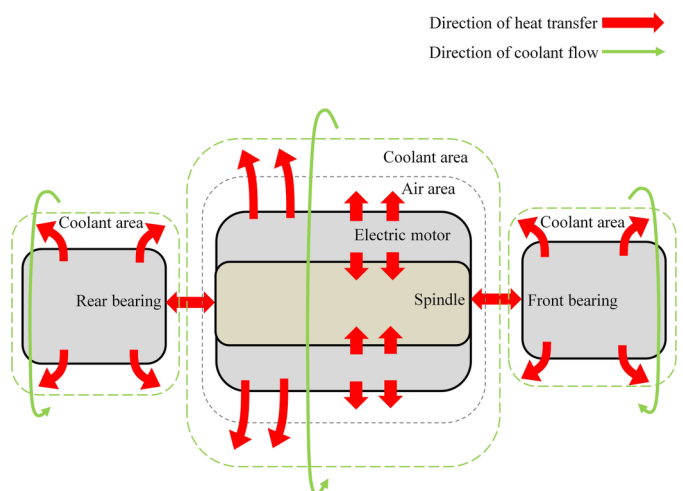


Fig. 1. Heat transfer process of electric spindle unit

It is assumed that the effect of the change in ambient temperature is not considered. According to the law of energy conservation, the rela-

tionship between the energy field and the temperature field internal to the spindle unit can be expressed as follows:

$$\begin{aligned} \bar{\Phi}_{total} &= \bar{\Phi}_{pro} + \bar{\Phi}_{thr} - \bar{\Phi}_{dis} = c_{sol} \frac{dT}{dt} \\ \text{and } \bar{\Phi}_{thr} &= \bar{\theta} A \frac{dT}{dt} \end{aligned} \quad (1)$$

where  $\bar{\Phi}_{pro}$  is the component heat generation power,  $\bar{\Phi}_{thr}$  is the heat conduction through the continuous cross section of the spindle unit,  $\bar{\Phi}_{dis}$  is the coolant heat exchange power,  $c_{sol}$  is the specific heat capacity coefficient,  $t$  is the heat transfer time,  $\bar{\theta}$  is the thermal conductivity of the spindle unit, and  $A$  is the area of the heat exchange surface.

## 2.2. Thermal error modeling based on IA

Since the electric spindle unit consists of many heat generating components, the process of thermal error modeling can be categorized as following:

### 1) Front and rear bearing heat generation power modeling

The heat generation power of the bearings operating under the load is expressed as:

$$W_b = 1.047 \times 10^{-4} \omega \cdot (M_v + M_e) \quad (2)$$

where  $\omega$  is the angular velocity,  $M_v$  is the friction torque relevant to the viscous lubrication, and  $M_e$  is the friction torque which depends on the applied load.

### 2) Motor heat generation power modeling

The motor of the electric spindle unit is the driving device, and its heat generation power can be expressed as [29]:

$$\bar{\Phi}_M = \bar{\Phi}_{M1} + \bar{\Phi}_{M2} \quad (3)$$

where  $\bar{\Phi}_{M1}$  is the heat generation power of rotor, and  $\bar{\Phi}_{M2}$  is the heat generation power of stator.

In Eq. (3), the heat generation power  $\bar{\Phi}_M$  can be obtained from the following equation:

$$\begin{cases} \bar{\Phi}_{M1} = \frac{Q_1}{V_1} \\ \bar{\Phi}_{M2} = \frac{Q_2}{V_2} \end{cases} \quad (4)$$

where  $Q_1$  is the heat generation of rotor,  $Q_2$  is the heat generation of stator,  $V_1$  is the volume of rotor, and  $V_2$  is the volume of stator.

### 3) Coolant heat transfer coefficient modeling

Coolant is an important medium in the cooling process. The heat transfer process internal to the spindle unit contains three parts: the direct contact heat exchange between the rotating components and the ambient air; the heat exchange between the bearings and the coolant; and the heat exchange between the motor and the coolant. The heat transfer coefficient is expressed as follows:

$$\begin{aligned} h &= Nu \frac{\bar{\theta}}{l_a} \\ \text{and } Nu &= 0.133 Re^{2/3} Pr^{1/3} \end{aligned} \quad (5)$$

where  $Re$  is the Reynolds value,  $Pr$  is the Prandtl value, and  $l_a$  is the cross-sectional circumference of the spindle unit.

### 4) Optimization of heat generation power and heat transfer coefficient

Generally, there is a deviation between the theoretical values and practice values acquired from Eq. (2) to Eq. (5). To narrow the gap between them, the optimal heat generation power and heat transfer coefficient are found based on IA. The iterative optimization process of IA is implemented by the operators, including the operator for evaluating affinity, the operator for evaluating antibody concentration, and the operator for calculating the degree of excitation and so on.

The equation for parameter optimization can be written as:

$$\begin{cases} \hat{U}_{F\_B\_M} = k_{F\_B\_M}^U \times U_{F\_B\_M} + b_{F\_B\_M}^U \\ \hat{h}_{f\_n} = k_{f\_n}^h \times h_{f\_n} + b_{f\_n}^h \end{cases} \quad (6)$$

where  $U_{F\_B\_M}$  are the heat generation power of the front bearing, rear bearing and motor, respectively;  $h_{f\_n}$  are the forced and natural convection heat transfer coefficient, respectively;  $k_{F\_B\_M}^U$ ,  $k_{f\_n}^h$  are the proportionality factor of heat generation power and heat transfer coefficient, and  $b_{F\_B\_M}^U$ ,  $b_{f\_n}^h$  are the deviation modification factor of heat generation power and heat transfer coefficient.

The vector form of optimized variables can be written as:

$$\begin{aligned} \chi &= [\chi_1, \chi_2, \chi_3, \chi_4, \chi_5, \chi_6, \chi_7, \chi_8, \chi_9, \chi_{10}]^T \\ &= [k_{F\_B\_M}^U, b_{F\_B\_M}^U, k_{B\_B}^U, b_{B\_B}^U, k_{M}^U, b_{M}^U, k_{f\_n}^h, b_{f\_n}^h, k_n^h, b_n^h,] \end{aligned} \quad (7)$$

The affinity indicates the binding strength of the immune cells to the antigens, and the antibody affinity function based on the Euclidean distance is expressed as follows:

$$\text{aff}(q_i, q_j) = \sqrt{\sum_{k=1}^r (q_{i,k} - q_{j,k})^2} \quad (8)$$

where  $\text{aff}(q_i, q_j)$  is the affinity between antibodies,  $q_{i,k}$  and  $q_{j,k}$  are the  $k$ -th dimension of antibody  $i$  and the  $k$ -th dimension of antibody  $j$ , and  $r$  is the number of antibody dimension.

To solve the optimization problem in this paper, Eq. (8) can be transformed into:

$$\min f(\chi) = \min \sqrt{(T_F - T_F^*)^2 + (T_M - T_M^*)^2 + (T_B - T_B^*)^2} \quad (9)$$

where  $T_F$ ,  $T_M$  and  $T_B$  are the front bearing, rear bearing and motor simulation temperature, respectively; and  $T_F^*$ ,  $T_M^*$  and  $T_B^*$  are the front bearing, rear bearing and motor experimental temperature, respectively.

The antibody concentration reflects the quality of antibody population, and the high concentration indicates the presence of many similar individuals which inhibits the global optimization procedure. To guarantee individuals have the characteristics of diversity, the antibody concentration is defined as follows:

$$\begin{aligned} \text{Den}(q_i) &= \frac{1}{L} \sum_{j=1}^L S(q_i, q_j) \\ \text{and } S(q_i, q_j) &= \begin{cases} 1 & \text{aff}(q_i, q_j) < \delta_s \\ 0 & \text{aff}(q_i, q_j) \geq \delta_s \end{cases} \end{aligned} \quad (10)$$

where  $L$  is the population size,  $S(q_i, q_j)$  is the similarity between antibodies, and  $\delta_s$  is the similarity threshold.

The incentive degree is an evaluation indicator for antibodies considering both affinity and concentration, and then the next generation of antibodies is screened. It can be described as:

$$sim(q_i) = a \cdot aff(q_i) - b \cdot Den(q_i) \quad (11)$$

where  $sim(q_i)$  is the incentive degree of the antibodies  $g_i$ , and  $a, b$  are calculation parameters depending on the actual situation.

The cloning process was performed by selecting the antibodies with the high incentives in the antibody population, which is represented as follows:

$$T_C(q_i) = clone(q_i)_m \quad (12)$$

where  $clone(q_i)$  is the set consisting of  $m$  cloned antibodies identical to  $q_i$ , and  $m$  is the number of clones.

By updating the antibodies with low incentive degree in the population and replacing them with new antibodies generated randomly, the global search is achieved. The optimization process is shown in Fig. 2, which can be summarized as follows: the basic parameters are set such as the immune algebra  $G=200$ , the variation probability  $P_m=0.7$ , and the incentive degree factor  $\alpha=2$ ; the initial range of variation of the variables  $k$  and  $b$  are set, and the random values of  $k$  and  $b$  are dynamically generated for the calculation of Eq. (6); the values calculated by Eq. (6) are used in the finite element simulation, the simulated temperature values and the experimental temperature values are used for the calculation of Eq. (7); and the optimal values of  $k$  and  $b$  are obtained by circular iterations.

### 5) The finite element simulation of spindle unit

On fluid-solid contact surface, the heat generation and the heat transfer processes of the motor and bearings can be described as:

$$\frac{\partial}{\partial t} (\rho_{flu/sol} \vartheta_u) + \nabla \cdot [\bar{\mu} (\rho_{flu/sol} \vartheta_u + p)] = \nabla \cdot [k_{flu/sol} \nabla T + (\xi \bar{\mu})] + Q_v \quad (13)$$

where  $\vartheta_u$  is the energy carried per unit mass,  $k_{flu/sol}$  denotes the thermal conductivity of fluid and solid,  $\bar{\mu}$  denotes the vector of velocity,  $\xi$  is the tensor of stress,  $\nabla \cdot (\xi \bar{\mu})$  is the heat dissipation of the coolant induced by viscous friction,  $Q_v$  denotes the heat generation power of the motor and bearings, and  $\nabla \cdot (k \nabla T)$  denotes the heat transfer of solid, coolant and air heat convection.

### 2.3. Machining accuracy modeling based on MBS

MBS serves as a complete abstraction of complicated mechanical systems, which can abstract the four-axis machine tool to be a system with multiple independent bodies. The machining accuracy model is then established by determining the position relationship between each body. The kinematic model of the four-axis machine tool is shown in Fig. 3. Fig. 3(a) shows the overall structural model of the machine tool. Fig. 3 (b) shows the topological framework of the machine tool. Fig. 3(a) consists of eight typical bodies, represented by  $D_j$  ( $j=1, 2..8$ ). Two branches can be obtained: the bed ( $D_1$ ) -X-axis moving part ( $D_2$ ) -Y-axis moving part ( $D_3$ ) -spindle ( $D_4$ )-tool ( $D_5$ ) branch,

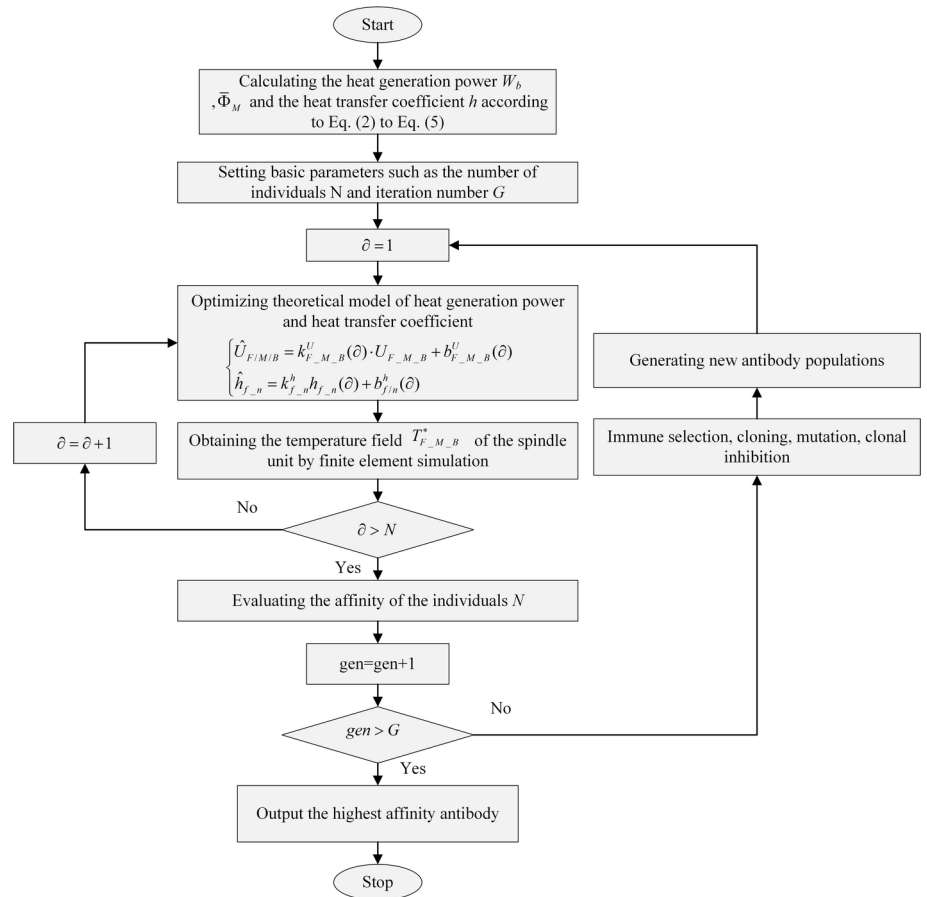


Fig. 2. Optimization process of immune algorithm

and the bed ( $D_1$ ) -Z-axis moving part ( $D_6$ ) -B-axis rotating part ( $D_7$ ) -workpiece ( $D_8$ ) branch.

The position change relationship between each two adjacent bodies is described by the homogeneous coordinate transformation matrices. The motion of any individual in the machine tool can be decomposed into two sub-motions, namely rotation around the axis and translation along the axis, so six errors are generated. Taking the Z-axis as an explanation, the matrix of error homogeneous transformation is written as follows:

$$\Delta \tilde{K}_{16s} = \begin{pmatrix} 1 & -\Delta \gamma_z & \Delta \beta_z & \Delta x_z \\ \Delta \gamma_z & 1 & -\Delta \alpha_z & \Delta y_z \\ -\Delta \beta_z & \Delta \alpha_z & 1 & \Delta z_z \\ 0 & 0 & 0 & 1 \end{pmatrix}$$

The four-axis machine tool includes X, Y, Z translation axes and B rotation axis. So a total of 30 geometric errors are generated. They are given in Table 1.

The forming point of the tool is in its own coordinate system as:

$$H_t = [H_{tx} \ H_{ty} \ H_{tz} \ 1]^T \quad (14)$$

Similarly, the forming point of the workpiece is in its own coordinate system as:

$$H_w = [H_{wx} \ H_{wy} \ H_{wz} \ 1]^T \quad (15)$$



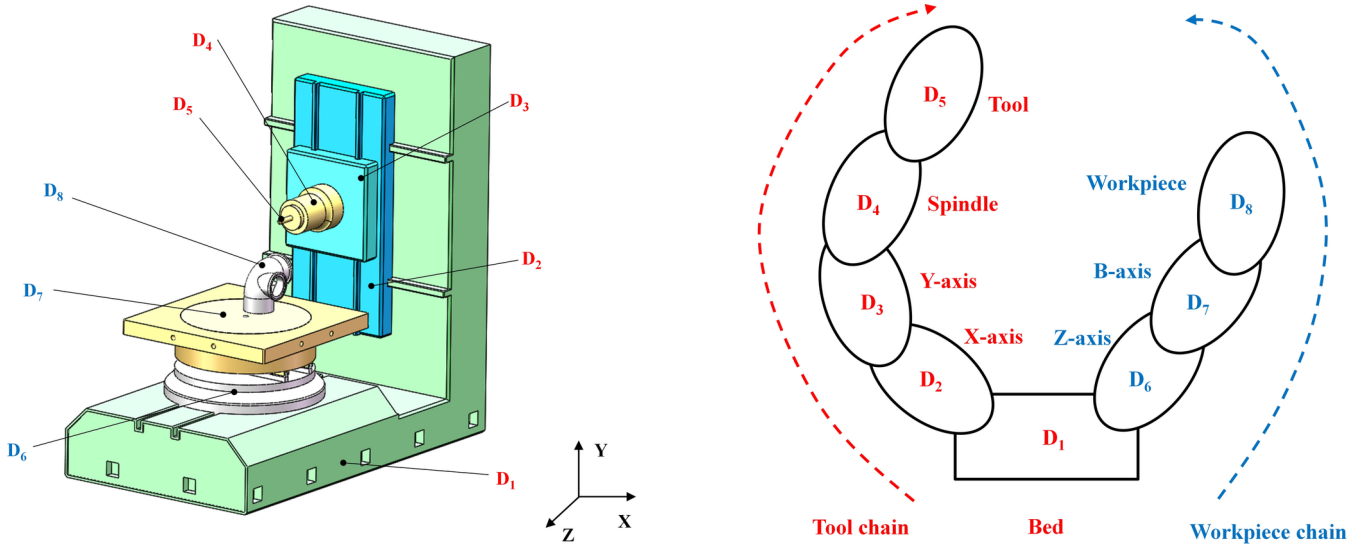


Fig. 3. The structural model and topological structure diagram of a four-axis machine tool platform

Table 1. Explanation of related symbols

Symbol	Definition
$\Delta x_x, \Delta y_y, \Delta z_z$	Positioning error
$\Delta x_y, \Delta x_z$	Straightness error in X-direction
$\Delta y_x, \Delta y_z$	Straightness error in Y-direction
$\Delta z_x, \Delta z_y$	Straightness error in Z-direction
$\Delta \alpha_x, \Delta \beta_y, \Delta \gamma_z$	Roll error
$\Delta \beta_x, \Delta \alpha_y, \Delta \alpha_z$	Pitch error
$\Delta \gamma_x, \Delta \gamma_y, \Delta \beta_z$	Yaw error
$\Delta x_B, \Delta y_B, \Delta z_B$	Run-out error in X-, Y-, Z-direction
$\Delta \alpha_B, \Delta \beta_B, \Delta \gamma_B$	Turning error
$S_{XY}, S_{XZ}, S_{YZ}$	Perpendicularity error
$\varepsilon \gamma_{yB}, \varepsilon \alpha_{xB}$	Parallelism error of B-axis in the XZ, YZ plane
$\varepsilon z_{yB}$	Offset error
$\Delta \varphi_x^T, \Delta \varphi_y^T, \Delta \varphi_z^T$	Thermal error along the X, Y, Z-direction

Ideally, their forming point coordinates in their own coordinate systems will overlap, so the machining accuracy can be written as:

$$\tilde{K}_{16p} \tilde{K}_{16s} \tilde{K}_{67p} \tilde{K}_{67s} \tilde{K}_{78p} \tilde{K}_{78s} \mathbf{H}_w = \tilde{K}_{12p} \tilde{K}_{12s} \tilde{K}_{23p} \tilde{K}_{23s} \tilde{K}_{34p} \tilde{K}_{34s} \tilde{K}_{45p} \tilde{K}_{45s} \mathbf{H}_t \quad (16)$$

where  $p, s$  are the static state and motion state, and  $\tilde{K}_{ijp}, \tilde{K}_{ijs}, i, j = 1, 2, \dots$  are the homogeneous transformation matrices of static and motion in the ideal state, respectively.

The workpiece forming point in an ideal state can be represented by the tool forming point as:

$$\mathbf{H}_t = (\tilde{K}_{12p} \tilde{K}_{12s} \tilde{K}_{23p} \tilde{K}_{23s} \tilde{K}_{34p} \tilde{K}_{34s} \tilde{K}_{45p} \tilde{K}_{45s})^{-1} \tilde{K}_{16p} \tilde{K}_{16s} \tilde{K}_{67p} \tilde{K}_{67s} \tilde{K}_{78p} \tilde{K}_{78s} \mathbf{H}_w \quad (17)$$

However, in practice, the geometric and the thermal errors can both affect the machining accuracy. The homogeneous transformation matrices between adjacent bodies are given in Table 2.

In summary, the machining accuracy model in the state of actual machining can be written as:

$$\mathbf{E} = \tilde{K}_{16p} \Delta \tilde{K}_{16p} \tilde{K}_{16s} \tilde{K}_{67p} \Delta \tilde{K}_{67p} \tilde{K}_{67s} \tilde{K}_{78p} \Delta \tilde{K}_{78p} \tilde{K}_{78s} \tilde{K}_{78s} \mathbf{H}_w - \tilde{K}_{12p} \Delta \tilde{K}_{12p} \tilde{K}_{12s} \tilde{K}_{23p} \Delta \tilde{K}_{23p} \tilde{K}_{23s} \tilde{K}_{34p} \Delta \tilde{K}_{34p} \tilde{K}_{34s} \tilde{K}_{45p} \Delta \tilde{K}_{45p} \tilde{K}_{45s} \mathbf{H}_t \quad (18)$$

where  $\Delta \tilde{K}_{ijp}$  and  $\Delta \tilde{K}_{ijs}, i, j = 1, 2, \dots$  are the homogeneous transformation matrices of the static error and motion error, respectively.

### 3. Machining accuracy reliability analysis based on LHSMC

#### 3.1. Preliminary

The machining accuracy reliability of the machine tool reflects its ability to achieve a specific function under specified conditions in a predetermined time period [26]. Here, it is regarded as a criterion to evaluate the merits of the four-axis machine tool. Besides, a machining accuracy reliability prediction method is presented based on LHSMC.

The process of LHSMC can be organized as follows: The sample size is determined by Latin hypercube sampling (LHS); the cumulative distribution curve is divided into equal intervals on the cumulative possibility scale [0, 1]; the samples are drawn from each interval of the possibility distribution and used to represent the value of each interval; and the values are used to reconstruct the possibility distribution of the variables.

The steps of drawing  $K$  samples  $\mathbf{v} = (v_{i1}, v_{i2}, \dots, v_{in})^T (i = 1, 2, \dots, K)$  from a random vector  $\mathbf{V} = (V_1, V_2, \dots, V_K)^T$  using LHS is as follows:

(1) The range of each random variable  $V_j (j = 1, 2, \dots, n)$  is divided into  $K$  equal probability intervals, which means that the range [0, 1] of the cumulative distribution function  $F_{V_j}(v_j)$  of variable  $V_j$  is divided into  $K$  non-overlapping subintervals  $[0, 1/K], [1/K, 2/K], \dots, [(K-1)/K, 1]$ .

(2) One sample is extracted from each of the  $K$  subintervals as to variable  $V_j$ . Then, only one random number is generated as to each interval, and it is taken as the representative value of the interval. As to the  $i$ -th interval,  $u_i = (i-1+u)/K$  when the representative value  $u_i$  is chosen randomly and the random number  $u$  is generated in  $U$

Table 2. Homogeneous transformation matrices of the four-axis CNC machine tool

Adjacent body number	Body ideal static, motion HTMs ( $\tilde{K}_{ijp}, \tilde{K}_{ijs}$ )	Body static, motion error HTMs ( $\Delta\tilde{K}_{ijp}, \Delta\tilde{K}_{ijs}$ )
1-2 X-axis	$\tilde{K}_{12p} = I_{4 \times 4}$	$\Delta\tilde{K}_{12p} = \begin{pmatrix} 1 & -S_{xy} & S_{xz} & 0 \\ S_{xy} & 1 & 0 & 0 \\ -S_{xz} & 0 & 1 & 0 \\ 0 & 0 & 0 & 1 \end{pmatrix}$
	$\tilde{K}_{12s} = \begin{pmatrix} 1 & 0 & 0 & x \\ 0 & 1 & 0 & 0 \\ 0 & 0 & 1 & 0 \\ 0 & 0 & 0 & 1 \end{pmatrix}$	$\Delta\tilde{K}_{12s} = \begin{pmatrix} 1 & -\Delta\gamma_x & \Delta\beta_x & \Delta x_x \\ \Delta\gamma_x & 1 & -\Delta\alpha_x & \Delta y_x \\ -\Delta\beta_x & \Delta\alpha_x & 1 & \Delta z_x \\ 0 & 0 & 0 & 1 \end{pmatrix}$
2-3 Y-axis	$\tilde{K}_{23p} = I_{4 \times 4}$	$\Delta\tilde{K}_{23p} = I_{4 \times 4}$
	$\tilde{K}_{23s} = \begin{pmatrix} 1 & 0 & 0 & 0 \\ 0 & 1 & 0 & y \\ 0 & 0 & 1 & 0 \\ 0 & 0 & 0 & 1 \end{pmatrix}$	$\Delta\tilde{K}_{23s} = \begin{pmatrix} 1 & -\Delta\gamma_y & \Delta\beta_y & \Delta x_y \\ \Delta\gamma_y & 1 & -\Delta\alpha_y & \Delta y_y \\ -\Delta\beta_y & \Delta\alpha_y & 1 & \Delta z_y \\ 0 & 0 & 0 & 1 \end{pmatrix}$
1-6 Z-axis	$\tilde{K}_{16p} = I_{4 \times 4}$	$\Delta\tilde{K}_{16p} = \begin{pmatrix} 1 & 0 & 0 & 0 \\ 0 & 1 & -S_{yz} & 0 \\ 0 & S_{yz} & 1 & 0 \\ 0 & 0 & 0 & 1 \end{pmatrix}$
	$\tilde{K}_{16s} = \begin{pmatrix} 1 & 0 & 0 & 0 \\ 0 & 1 & 0 & 0 \\ 0 & 0 & 1 & z \\ 0 & 0 & 0 & 1 \end{pmatrix}$	$\Delta\tilde{K}_{16s} = \begin{pmatrix} 1 & -\Delta\gamma_z & \Delta\beta_z & \Delta x_z \\ \Delta\gamma_z & 1 & -\Delta\alpha_z & \Delta y_z \\ -\Delta\beta_z & \Delta\alpha_z & 1 & \Delta z_z \\ 0 & 0 & 0 & 1 \end{pmatrix}$
6-7 B-axis	$\tilde{K}_{67p} = I_{4 \times 4}$	$\Delta\tilde{K}_{67p} = \begin{pmatrix} 1 & -\Delta\gamma_{xB} & 0 & 0 \\ \Delta\gamma_{xB} & 1 & -\Delta\alpha_{zB} & 0 \\ 0 & \Delta\alpha_{zB} & 1 & \Delta z_{yB} \\ 0 & 0 & 0 & 1 \end{pmatrix}$
	$\tilde{K}_{67s} = \begin{pmatrix} \cos B & 0 & \sin B & 0 \\ 0 & 1 & 0 & 0 \\ -\sin B & 0 & \cos B & 0 \\ 0 & 0 & 0 & 1 \end{pmatrix}$	$\Delta\tilde{K}_{67s} = \begin{pmatrix} 1 & -\Delta\gamma_B & \Delta\beta_B & \Delta x_B \\ \Delta\gamma_B & 1 & -\Delta\alpha_B & \Delta y_B \\ -\Delta\beta_B & \Delta\alpha_B & 1 & \Delta z_B \\ 0 & 0 & 0 & 1 \end{pmatrix}$
7-8 Workpiece	$\tilde{K}_{78p} = \begin{pmatrix} 1 & 0 & 0 & x_w \\ 0 & 1 & 0 & y_w \\ 0 & 0 & 1 & z_w \\ 0 & 0 & 0 & 1 \end{pmatrix}$	$\Delta\tilde{K}_{78p} = I_{4 \times 4}$
	$\tilde{K}_{78s} = I_{4 \times 4}$	$\Delta\tilde{K}_{78s} = I_{4 \times 4}$
4-5 Tool	$\tilde{K}_{45p} = \begin{pmatrix} 1 & 0 & 0 & x_t \\ 0 & 1 & 0 & y_t \\ 0 & 0 & 1 & z_t \\ 0 & 0 & 0 & 1 \end{pmatrix}$	$\Delta\tilde{K}_{45p} = I_{4 \times 4}$
	$\tilde{K}_{45s} = I_{4 \times 4}$	$\Delta\tilde{K}_{45s} = I_{4 \times 4}$
3-4 Spindle	$\tilde{K}_{34p} = I_{4 \times 4}$	$\Delta\tilde{K}_{34p} = I_{4 \times 4}$
	$\tilde{K}_{34s} = I_{4 \times 4}$	$\Delta\tilde{K}_{34s} = \begin{pmatrix} 1 & 0 & 0 & \Delta\varphi_x^T \\ 0 & 1 & 0 & \Delta\varphi_y^T \\ 0 & 0 & 1 & \Delta\varphi_z^T \\ 0 & 0 & 0 & 1 \end{pmatrix}$

(0, 1); and  $u_i = (i - 1/2) / K$  when it is selected at the center of the interval.

(3) The  $K$  sample values of variable  $V_j$  are randomly sorted according to the ordinal number of the interval to which they belong, and they are placed together in the order of the variables. It is equivalent to constructing a sampling ordinal matrix  $\mathbf{R} = [r_{ij}]_{K \times n}$  with  $K$  rows and  $n$  columns. Besides, the variables are in the column order, and each column is a random and unique arrangement of the ordinal numbers 1, 2, ...,  $K$ , and the  $K$  samples of each variable are arranged by numbers in the columns.

The sequential matrix  $\mathbf{R}$  is randomly generated, and the columns which introduce the statistical correlations affect the simulation results. The Spearman coefficient of the order matrix  $\mathbf{R}$  is employed to reduce the statistical correlation, described by  $\rho_S = [q_{ijs}]_{n \times n}$ . The Spearman rank correlation coefficients of the  $i$ -th and  $j$ -th columns can be obtained by:

$$q_{ijs} = 1 - \frac{6}{K(K^2 - 1)} \sum_{a=1}^K (r_{ai} - r_{aj})^2 \quad (19)$$

where  $q_{ijs}$  is a symmetric matrix, and it is equal to the unit matrix  $\mathbf{I}_n$  in the case of uncorrelated columns. There are no columns with the same sort in  $\mathbf{R}$ , so the matrix  $\rho_S$  is positive definite.

The LHSMC reflects the variable distribution characteristics by using the few samples, which can effectively simulate the failure possibility of machine tools.

### 3.2. Machining accuracy reliability analysis

When a part of the machine structure or the whole exceeds the specified state and cannot operate in accordance with the desired functional requirements, the specified state is a limit state which is critical to judge the structure reliability [28]. To analyze the structure reliability, it is necessary to determine whether it has reached its limit state. This section studied the machining accuracy reliability under the stochastic uncertainty of errors, and the performance function is represented as:

$$\eta = g(\zeta) = (\zeta_1, \zeta_2, \dots, \zeta_n) \quad (20)$$

In Eq. (20),  $\zeta = (\zeta_1, \zeta_2, \dots, \zeta_n)^T$  contains the  $n$  basic random variables affecting the machining accuracy reliability,  $\eta < 0$  means the structure is in a failure state, and  $\eta = 0$  means the structure is in a limit state.

Function  $\eta$  is a continuous random variable, and the failure possibility can be expressed as:

$$p_f = P(\eta \leq 0) = \int_{-\infty}^0 f_\eta(z) dz = F_\eta(0) \quad (21)$$

where  $f_\eta(z)$  is the possibility density function of  $\eta$ , and  $F_\eta(z)$  is the cumulative distribution function of  $\eta$ .

Also, the failure possibility can be written as:

$$p_f = \int_{\eta \leq 0} dF_\zeta(\kappa) = \int_{\eta \leq 0} f_\zeta(\kappa) d\kappa = \int \dots \int_{\eta \leq 0} f_\zeta(\kappa_1, \kappa_2, \dots, \kappa_n) d\kappa_1 d\kappa_2 \dots d\kappa_n \quad (22)$$

where  $f_\zeta(\kappa) = f_\zeta(\kappa_1, \kappa_2, \dots, \kappa_n)$  is the joint possibility density function of variable  $\zeta = (\zeta_1, \zeta_2, \dots, \zeta_n)^T$ , and  $F_\zeta(\kappa) = F_\zeta(\kappa_1, \kappa_2, \dots, \kappa_n)$  is the joint cumulative distribution function of random variable  $\zeta = (\zeta_1, \zeta_2, \dots, \zeta_n)^T$ .

However, the joint possibility density function  $f_\zeta(\kappa)$  is hard to obtain. From Eq. (21),  $p_f$  is determined by the form of the distribution of the functional function  $\eta$ . Assuming  $\eta$  obeys normal distribution, its mean value and standard deviation are  $\bar{\mu}_\eta$  and  $\bar{\sigma}_\eta$ , which is denoted as  $\eta \sim N(\bar{\mu}_\eta, \bar{\sigma}_\eta)$ . Then, the possibility density function  $f_\eta(z)$  of  $\eta$  is expressed as:

$$f_N(z | \bar{\mu}_\eta, \bar{\sigma}_\eta) = \frac{1}{\sqrt{2\pi}\bar{\sigma}_\eta} \exp\left(-\frac{(z - \bar{\mu}_\eta)^2}{2\bar{\sigma}_\eta^2}\right) \quad (23)$$

$\eta$  is converted to a standard normal distribution variable  $K \sim N(0, 1)$  by  $K = (\eta - \bar{\mu}_\eta) / \bar{\sigma}_\eta$ , and the possibility density function and cumulative distribution function can be expressed as:

$$\begin{cases} \phi(\tilde{k}) = \frac{1}{\sqrt{2\pi}} \exp\left(-\frac{\tilde{k}^2}{2}\right) \\ \omega(\tilde{k}) = \int_{-\infty}^k \phi(\tilde{k}) d\tilde{k} \end{cases} \quad (24)$$

According to Eq. (24), if the variable  $\eta$  is normally distributed, its possibility density and cumulative distribution functions are transformed into:

$$\begin{cases} f_N(z | \bar{\mu}_\eta, \bar{\sigma}_\eta) = \frac{1}{\bar{\sigma}_\eta} \phi\left(\frac{z - \bar{\mu}_\eta}{\bar{\sigma}_\eta}\right) \\ F_N(z | \bar{\mu}_\eta, \bar{\sigma}_\eta) = \omega\left(\frac{z - \bar{\mu}_\eta}{\bar{\sigma}_\eta}\right) \end{cases} \quad (25)$$

Then, the failure possibility can be described by the following equation:

$$p_f = F_N(0 | \bar{\mu}_\eta, \bar{\sigma}_\eta) = \omega\left(-\frac{\bar{\mu}_\eta}{\bar{\sigma}_\eta}\right) \quad (26)$$

Up to now, a machining accuracy reliability analysis method for the machine tool based on LHSMC is formed. The proposal procedure of the method is illustrated in Fig. 4.

## 4. A case demonstration

### 4.1. Validation of thermal error

The four-axis machine tool is taken as a research example, and its basic parameters are given in Table 3. Through analyzing the heat generation mechanism, the heat generation power and heat transfer coefficient were determined as the characteristic parameters related to the thermal error. Then, they were optimized by IA, and they were employed as the thermal load and boundary conditions of the steady-state thermal analysis of the electric spindle unit in finite element analysis software.

Table 3. Basic parameters of the machine tool

Parameter type	Value
Length × Width × Height	6775mm × 4500mm × 4370mm
Spindle speed	80-8000r/min
Motor power	22kW
Movable distance in X-axis	1400mm

Movable distance in Y-axis	1000mm
Movable distance in Z-axis	900mm
B-axis rotation	0°-360°

The electric spindle unit is assembled from many parts. Inevitably, there are small features inside the spindle unit. To decrease the complexity of the simulation, the spindle system was simplified by ignoring small chamfers, mounting holes and screw holes. The interference fit between parts is not considered. The bearing balls are regarded as rings for finite element simulation purpose. The simplified spindle unit is shown in Fig. 5(a), and Fig. 5(b) shows the half-section

structure of the spindle unit, which shows the internal components and position relationship of the spindle unit. The three-dimensional model of the spindle unit is imported into the analysis software, and its finite element mesh model is obtained by the automatic mesh division method, as shown in Fig. 5(c) and Fig. 5(d). In addition, the material of the spindle unit structure is defined in the material library of analysis software.

The following conditions are set before performing the steady-state thermal temperature field simulation: the material parameters of each component of the electric spindle are set; the environmental and coolant inlet temperature are set at 20°C; the coolant flow rate is set at 5L/min as a constant; the optimized heat generation power is applied to the motor and bearings as the heat source, and the optimized heat transfer coefficient is applied to the heat transfer surface as the boundary condition. The simulation process is in the steady-state thermal analysis module of the analysis software.

The temperature field distribution of spindle unit in the thermal steady state is shown in Fig. 6. Fig. 6(a) shows the temperature field distribution of main components of the spindle unit. The highest temperature and the lowest temperature of the body are 33.09°C and 20.52°C, respectively. The temperature in the middle of the cooling jacket is higher than the two ends, which is related to the direct contact between the cooling jacket and the heat source. Fig. 6(b) shows the temperature distribution of the heat generating parts such as rotor, stator and bearings of the spindle unit. Fig. 6(c) shows the internal temperature distribution of the spindle unit, which implies the internal heat accumulation in the thermal steady state.

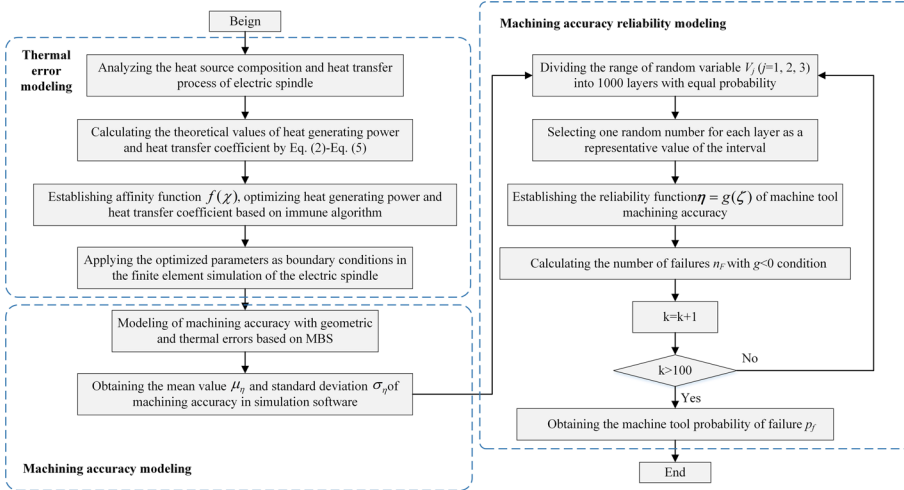


Fig. 4. Flow chart for machining accuracy reliability analysis of the four-axis machine tool

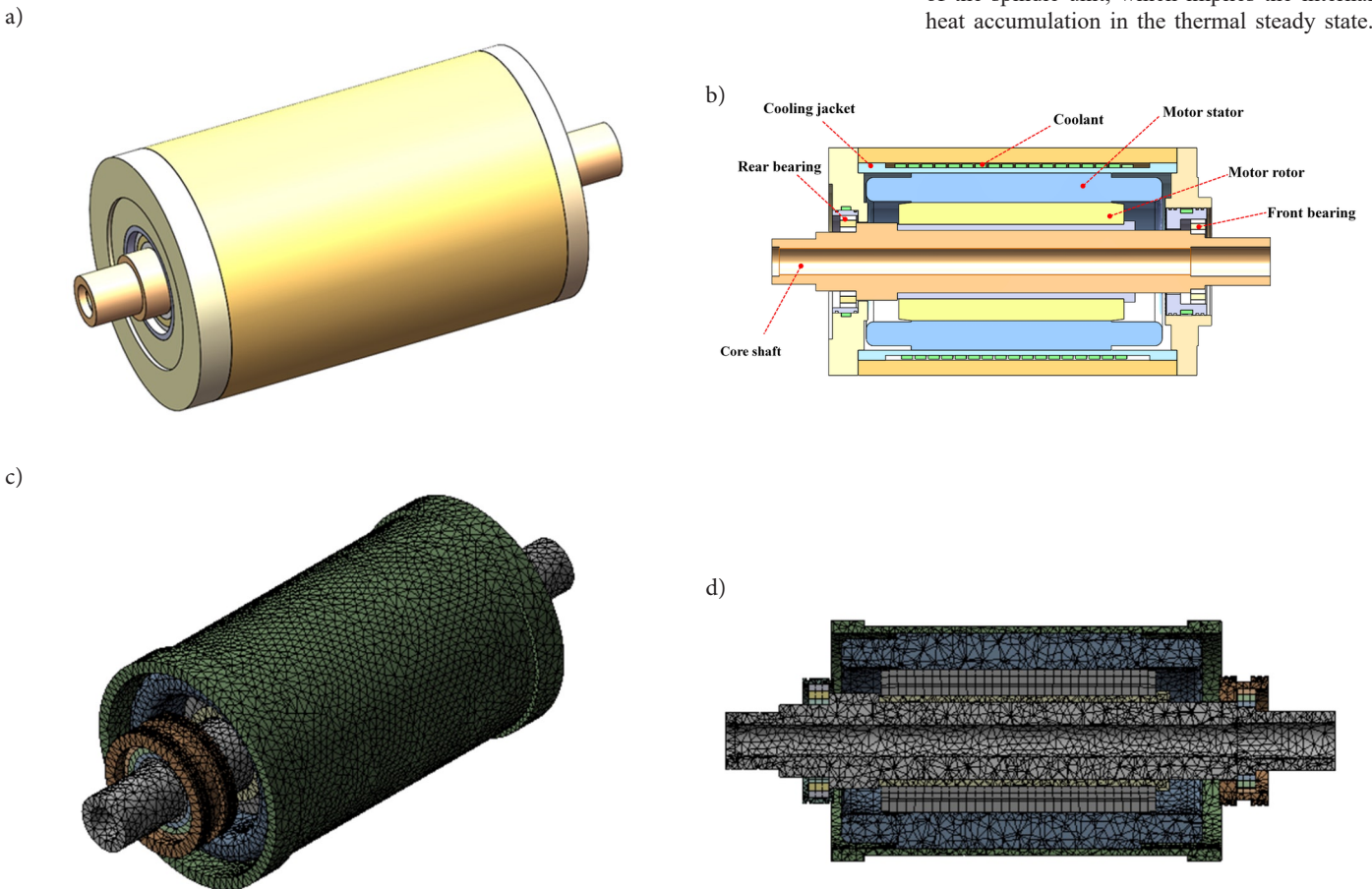


Fig. 5. The finite element model of the spindle unit: a) the overall structure of the electric spindle, b) the half-section structure of the electric spindle, c) the finite element mesh model of main components, d) the section view of finite element mesh model of main components



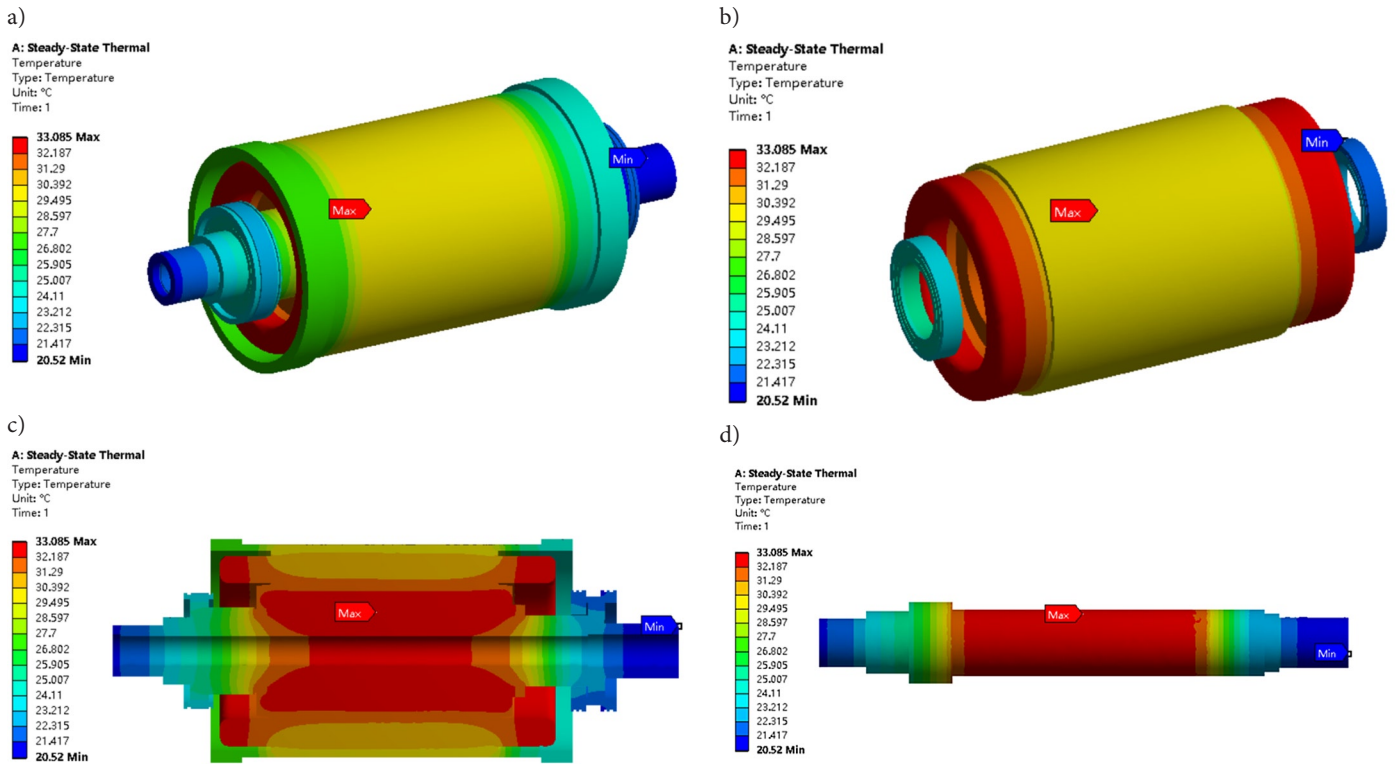


Fig. 6. Temperature distribution of the spindle unit in thermal steady state: a) the temperature field of main components, b) the temperature field of heat generating components, c) the internal temperature field of the electric spindle, d) the temperature field of the core shaft

Fig. 6(d) shows the temperature distribution and characteristic of the core shaft, the highest temperature (33.09°C) occurs in the middle part of the core shaft.

The temperature prediction values and the experimental values based on Particle swarm optimization algorithm (PSO) and IA are given in Table 4. The two methods are both used to optimize the characteristic parameters.

Table 4 indicates that the temperature rise of different components of the spindle unit was predicted based on IA with less error than PSO, which explains the thermal error modeling based on IA has better prediction effect.

Table 4. The comparison between predicted temperature and experimental temperature

Location	Experimental value (°C)	Prediction value based on IA (°C)	Error%	Prediction value based on PSO (°C)	Error%
Front bearing	22.9	24.8	7.66	26.1	12.26
Rear bearing	21.5	23.6	8.90	24.6	12.60
Motor	27.5	29.5	6.78	30.8	10.71

The temperature field model was imported into the finite element mechanics analysis module, and the fixed constraints were configured. The deformation of the electric spindle unit was obtained as shown in Fig. 7 and Fig. 8.

Fig. 7(a) shows the total deformation distribution of the spindle unit, and the maximum deformation is 1.7446e-5m. The max deformation along the X-, Y- and Z-directions are 1.6799e-5m, 6.5465e-6m and 6.6051e-6m, as shown in Fig. 7(b)-(d). Fig. 8 shows the axial deformation of the core shaft is 1.3078e-5m.

## 4.2. Validation of machining accuracy

The machining accuracy model comprising the geometric and thermal errors was developed in the paper. To validate the model, the thermal deformation of the core shaft was extracted directly from the finite element simulation results as the thermal error. 30 geometric errors of the machine tool were measured by the relevant measuring

instruments. Fig. 9 shows the platform and workpiece of the four-axis CNC machine tool. 30 measuring points are selected from the workpiece coordinate system, and their coordinates are:

$$(x, y, 1)(x = 50, 150, 250, 350, 450, 550, y = 100, 200, 300, 400, 500).$$

The machining accuracy of each point is calculated based on MBS, and the results are shown in Fig. 10.

Fig. 10 describes the predicted and measured values of the machining accuracy in the X-, Y- and Z-directions, respectively, which illustrates that the machining accuracy with thermal error exhibits less deviations from the measured machining accuracy. Hence, the thermal error model established in the paper is verified.

## 4.3. Validation of machining accuracy reliability

The distribution characteristics of errors need to be determined before discussing the machine tools reliability. Normally, the geometric errors are regarded as Gaussian distribution [26]. These 30 measuring points are employed to predict the machining accuracy reliability.

To predict the machining accuracy reliability at different coordinates, the Monte Carlo method was used as the simulation standard. The LHSMC and the AFOSM methods were used as the prediction methods, and the deviation of their reliability prediction values from Monte Carlo was shown in Fig. 11.

Fig. 11 demonstrates that the prediction value of machining accuracy reliability obtained by LHSMC, AFOSM and Monte Carlo, respectively. It can be noted that the reliability prediction value of LHSMC is closer to Monte Carlo than AFOSM. The results illustrate that the LHSMC method in predicting the machining accuracy reliability has a higher accuracy compared with AFOSM.

To verify the machining accuracy reliability analysis method proposed in this paper, the coordinates covering the entire workpieces are selected according to the dimensions of the workpieces. A total of 300 workpieces are machined, as shown in Fig. 12. The failure possibility

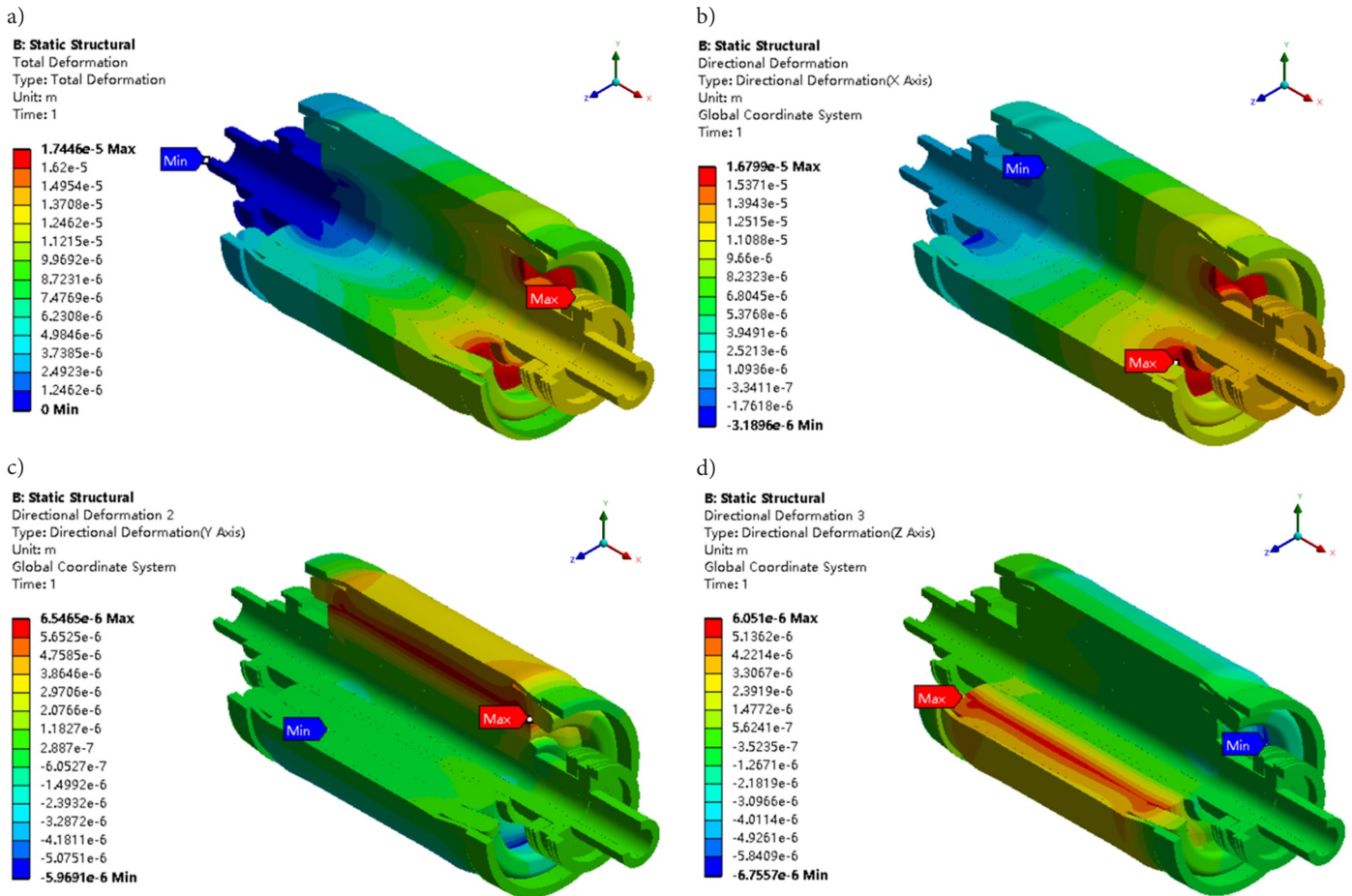


Fig. 7. Thermal deformation nephogram of the spindle unit, a) the total deformation, b) the deformation in X-direction, c) the deformation in Y-direction, d) the deformation in Z-direction

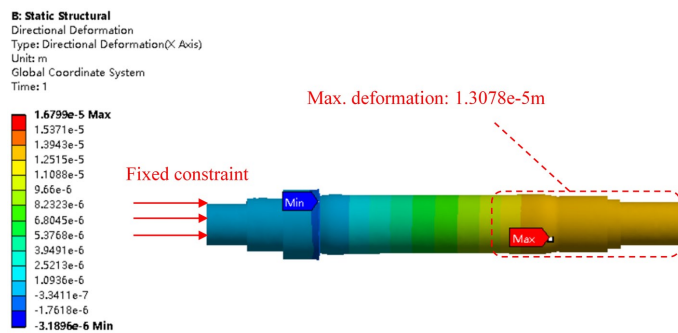


Fig. 8. Axial deformation of the core shaft

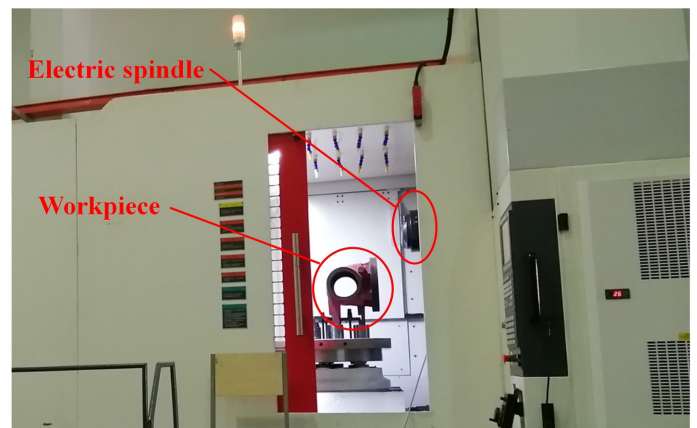


Fig. 9. Four-axis CNC machining tool platform

is calculated as the experimental data of machining accuracy reliability. The results are shown in Table 5.

Table 5 shows the predicted values of machining accuracy reliability based on different methods, and the comparison with the experimental values verifies that the machining accuracy reliability analysis method proposed in the paper has a higher accuracy than AFOSM.

## 5. Conclusion

CNC machine tools are high continuity equipment, and their machining accuracy reliability mainly is affected by the geometric and thermal errors. Therefore, a thermal error modeling and machining accuracy reliability analysis method is presented, and the detailed conclusions comprise as following:

1. Based on the heat generation mechanism and IA, a thermal error model was established, which was used to estimate the thermal error in the actual machining process of machine tools;
2. Applying the MBS theory, a machining accuracy model including both geometric and thermal errors was established to derive the machining accuracy of machine tools;
3. A machine accuracy reliability prediction method was put forward considering the spindle thermal error. The effectiveness and superiority of the method were experimentally demonstrated. It can provide the methodological support for spindle unit thermal error modeling and dynamic machining accuracy reliability prediction of machine tools.

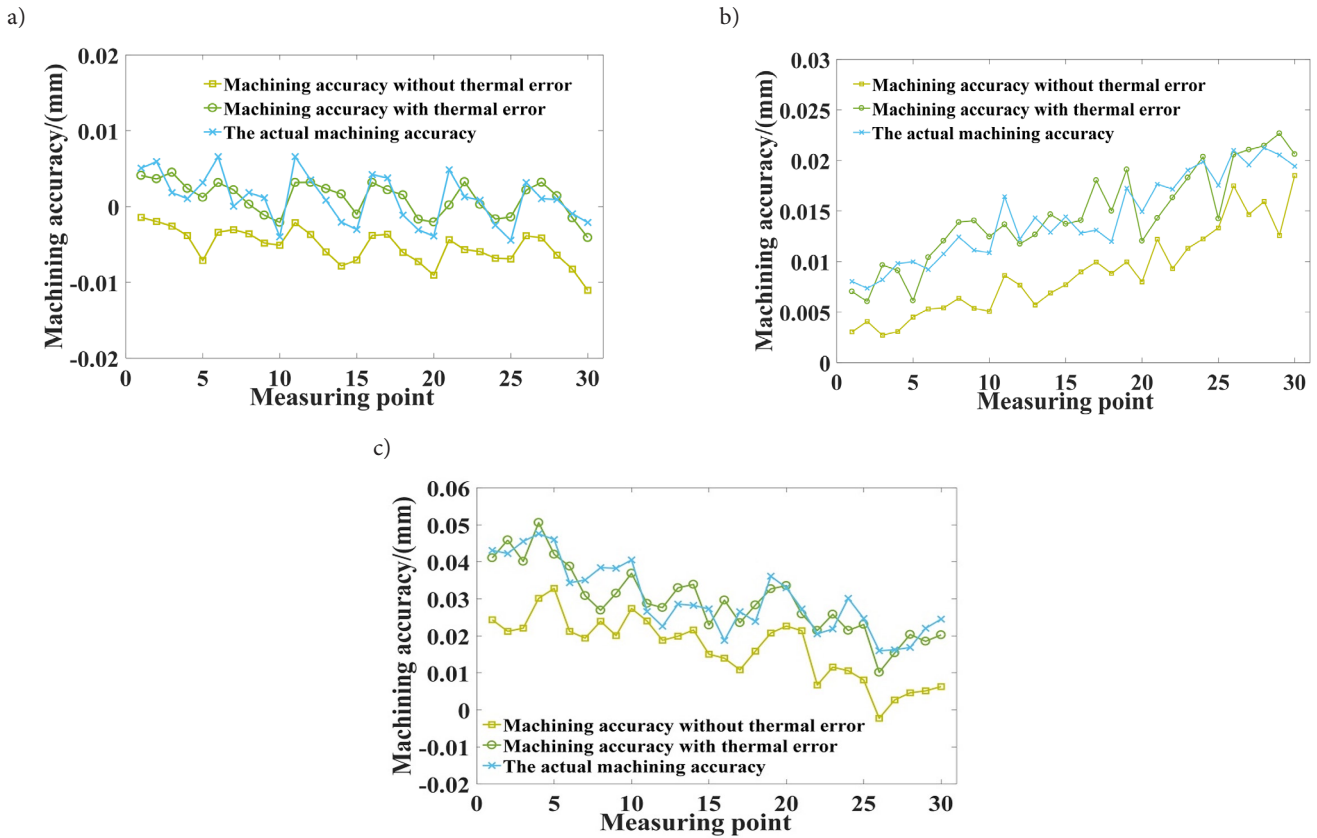


Fig. 10. Machining accuracy of 30 measuring points: a) machining accuracy in X-direction, b) machining accuracy in Y-direction, c) machining accuracy in Z-direction

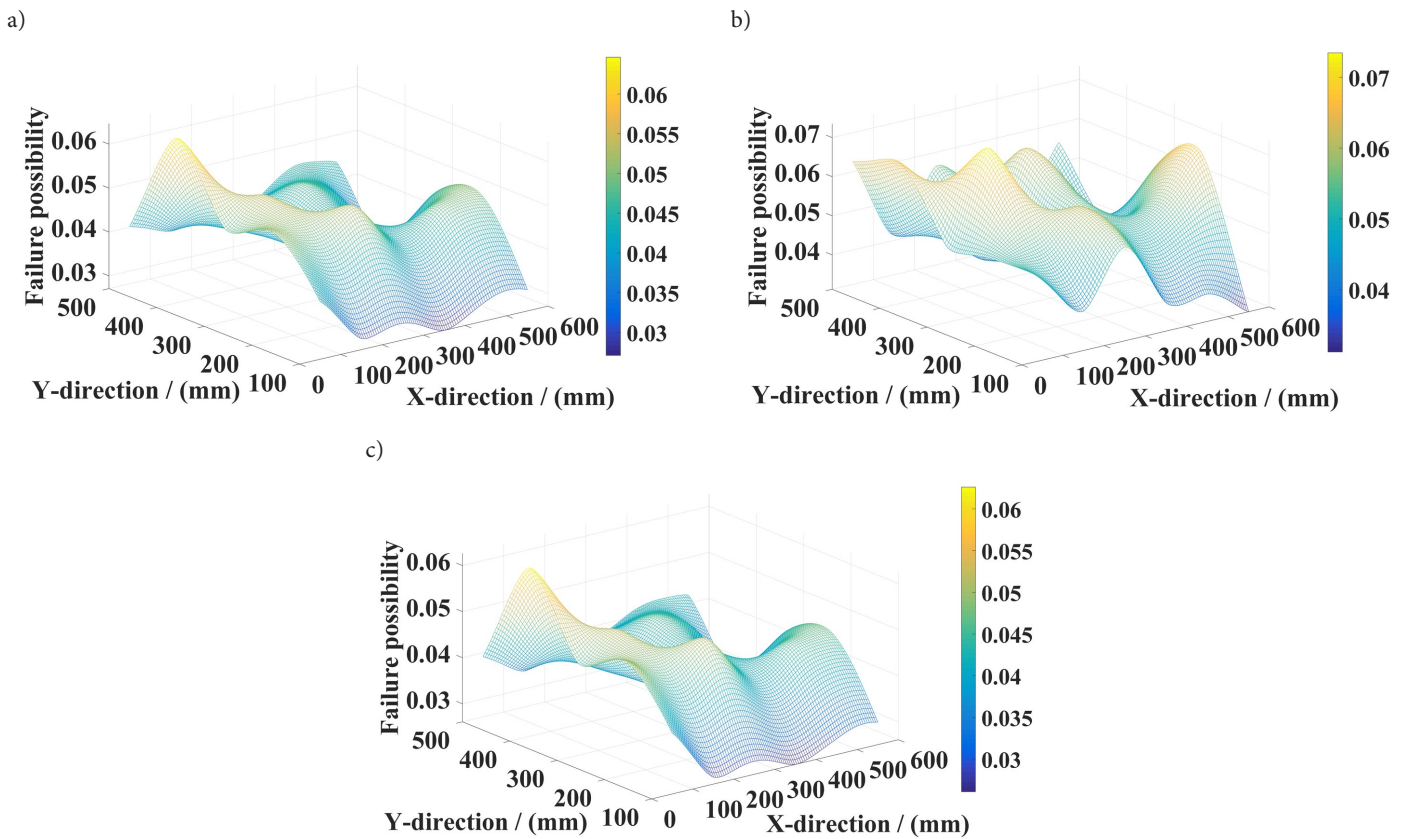


Fig. 11. Machining accuracy reliability of 30 measuring points: a) failure possibility based on LHSMC, b) failure possibility based on AFOSM, c) failure possibility based on Monte Carlo



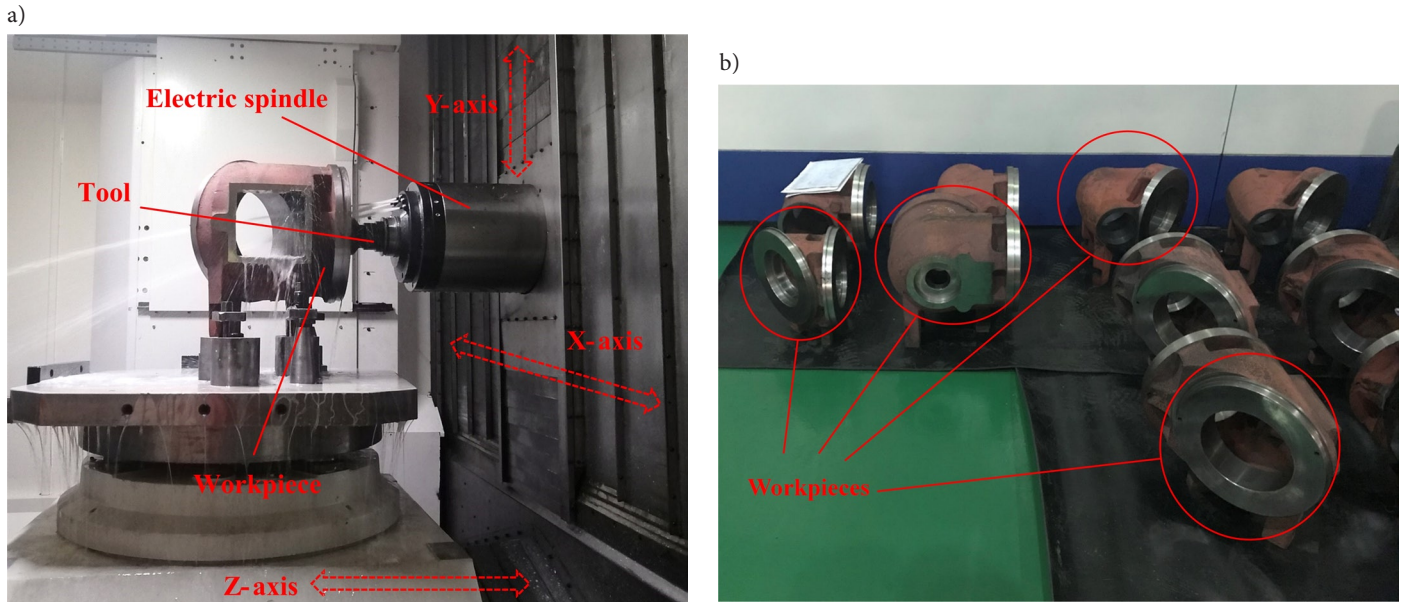


Fig. 12. The machining process of the workpieces: a) the machining process of a workpiece, b) various workpieces

Table 5. Failure possibility of measuring points obtained based on different methods

Coordinate of point (x, y)	Total number of workpieces	Number of failed workpieces	The failure possibility			
			Experimental value	Monte Carlo	LHSMC	AFOSM
(300,30)	300	9	3.00%	3.11%	3.25%	3.96%
(570,300)	300	11	3.67%	3.68%	3.84%	4.35%
(300,570)	300	13	4.33%	4.01%	4.32%	5.03%
(30,300)	300	10	3.33%	3.39%	3.58%	3.97%
(110,110)	300	8	2.67%	2.68%	2.53%	3.31%
(490,110)	300	9	3.00%	3.12%	3.05%	3.28%
(110,490)	300	10	3.33%	3.38%	3.46%	3.36%
(490,490)	300	14	4.67%	4.58%	4.72%	5.03%

#### Acknowledgements

The research was sponsored by the National Natural Science Foundation of China (grant no.51905334, grant no.51975012 and grant no.12002186), Shanghai Sailing Program (grant no.19YF1418600), Beijing Nova Programmer Interdisciplinary Cooperation Project (grant no. Z191100001119010), and the National Science and Technology Major Project (grant no.2018ZX04033001-003).

#### Appendix

Parameter	Equation	Value
$M_{v1}$ (N • mm) (Front bearing)	$M_{v1,v2} = 10^{-7} f^* (vn')^{2/3} d_{m1,m2}^3$ <p><math>f^*</math> denotes the coefficient related to bearing lubrication, and <math>f^* = 4</math>;  <math>v</math> denotes the lubricant kinematic viscosity, and <math>v = 45</math> (mm<sup>2</sup>/s);  <math>n'</math> denotes the bearing speed, and <math>n' = 8000</math> (r/min);</p>	1811.1
$M_{v2}$ (N • mm) (Rear bearing)	<p><math>d_{m1}</math> is the front bearing mean diameter, and <math>d_{m1} = 95</math>(mm);  <math>d_{m2}</math> is the rear bearing mean diameter, and <math>d_{m2} = 100.25</math> (mm)</p>	2128.3



$M_{e1}$ (N · mm) (Front bearing)	$M_{e1,e2} = f_{1,2}P_{1,2}d_{m1,m2}$ $f_{1,2}$ denotes the coefficient related to bearing type, and $f_1 = 0.0012$ , $f_2 = 0.001$ ; $P_{1,2}$ denotes the bearing equivalent dynamic load, and $P_1 = 65.8$ (KN), $P_2 = 81.5$ (KN)	7501.2
$M_{e2}$ (N · mm) (Rear bearing)		8987.4
$Q_1$ (w) (Rotor)	$Q_{1,2} = (1-\eta)K_{1,2}W_M$ $\eta$ is the power conversion efficiency of the motor, and $\eta = 0.85$ ; $K_{1,2}$ is the heat production proportion of rotor and stator, and $K_1 = 0.35$ , $K_2 = 0.65$ ;	1155
$Q_2$ (w) (Stator)	$W_M$ is the rated power of the motor, and $W_M = 22$ (kW)	2145
$V_1$ (m <sup>3</sup> ) (Rotor)	$V_{1,2} = \pi(r_{o1,o2} - r_{i1,i2})^2 h_{1,2}$ $r_{o1,o2}$ is the outer diameter of the rotor and stator, and $r_{o1} = 0.08$ (m), $r_{o2} = 0.12$ (m); $r_{i1,i2}$ is the inner diameter of the rotor and stator, and $r_{i1} = 0.05$ (m), $r_{i2} = 0.08$ (m);	0.000876
$V_2$ (m <sup>3</sup> ) (Stator)	$h_{1,2}$ is the length of the rotor and stator, and $h_1 = 0.31$ (m), $h_2 = 0.41$ (m)	0.0021
$\bar{\theta}$ (W/(m·°C))	$\bar{\theta}$ is the thermal conductivity of the spindle unit, and $\bar{\theta} = 45$ .	45
$l_a$ (m)	$l_a$ is the cross-sectional circumference of the motor cooling jacket, and $l_a = 0.7536$ .	0.7536
$Re$	$Re = \frac{u'd'}{v'}$ $u'$ is the coolant average flow rate, and $u' = 0.99$ (m/s) $d'$ is the cooling pipe diameter, and $d' = 0.006$ (m) $v'$ is the coolant kinematic viscosity, and $v' = 0.0008737/1000$ (m <sup>2</sup> /s)	6798
$Pr$	$Pr = \frac{\mu C_p}{k}$ $\mu$ is the dynamic viscosity of the coolant, and $\mu = 0.8937/1000$ (kg/s·m) $C_p$ is the specific heat at constant pressure of coolant, and $C_p = 4.18$ (kJ/kg·K) $k$ is the thermal conductivity of the coolant, and $k = 0.61$ (W/m·K)	6.12

## References

- Cai LG, Zhang ZL, Cheng Q, Liu ZF, Gu PH. A geometric accuracy design method of multi-axis NC machine tool for improving machining accuracy reliability. *Eksploracja i Niezawodność - Maintenance and Reliability* 2014; 17(1): 143–155, <https://doi.org/10.17531/ein.2015.1.19>.
- Cheng Q, Zhao HW, Zhao YS, Sun BW, Gu PH. Machining accuracy reliability analysis of multi-axis machine tool based on Monte Carlo simulation. *Journal of Intelligent Manufacturing* 2018; 29(1): 191–209, <https://doi.org/10.1007/s10845-015-1101-1>.
- Chen JX, Lin SW, Zhou XL. A comprehensive error analysis method for the geometric error of multi-axis machine tool. *International Journal of Machine Tools and Manufacture* 2016; 106: 56–66, <https://doi.org/10.1016/j.ijmactools.2016.04.001>.
- Cheng Q, Sun BW, Zhao YS, Gu PH. A method to analyze the machining accuracy reliability sensitivity of machine tools based on Fast Markov Chain simulation. *Eksploracja i Niezawodność - Maintenance and Reliability* 2016; 18(4): 552–564, <https://doi.org/10.17531/ein.2016.4.10>.
- Fu GQ, Fu JZ, Xu YT, Chen ZC, Lai JT. Accuracy enhancement of five-axis machine tool based on differential motion matrix: Geometric error modeling, identification and compensation. *International Journal of Machine Tools and Manufacture* 2015; 89: 170–181, <https://doi.org/10.1016/j.ijmactools.2014.11.005>.
- Hou RS, Yan ZZ, Du HY, Chen T, Tao T, Mei XS. The Application of Multi-objective Genetic Algorithm in the Modeling of Thermal Error of NC Lathe. *Procedia CIRP* 2018; 67: 332–337, <https://doi.org/10.1016/j.procir.2017.12.222>.
- Huang YB, Fan KC, Lou ZF, Sun W. A novel modeling of volumetric errors of three-axis machine tools based on Abbe and Bryan principles. *International Journal of Machine Tools and Manufacture* 2020; 151: 103527, <https://doi.org/10.1016/j.ijmactools.2020.103527>.
- Jiang ZY, Huang XZ, Chang MX, Li C, Ge Y. Thermal error prediction and reliability sensitivity analysis of motorized spindle based on

- Kriging model. *Engineering Failure Analysis* 2021; 127: 105558, <https://doi.org/10.1016/j.engfailanal.2021.105558>.
9. Kiridena V, Ferreira PM. Mapping the effects of positioning errors on the volumetric accuracy of five-axis CNC machine tools. *International Journal of Machine Tools and Manufacture* 1993; 33(3): 417–437, [https://doi.org/10.1016/0890-6955\(93\)90049-Z](https://doi.org/10.1016/0890-6955(93)90049-Z).
  10. Kwintarini W, Wibowo A, Martawirya YY. Mathematical approach for geometric error modeling of three axis CNC vertical milling machine. *Applied Mechanics and Materials* 2016; 842: 303–310, <https://doi.org/10.4028/www.scientific.net/AMM.842.303>.
  11. Li B, Tian XT, Zhang M. Thermal error modeling of machine tool spindle based on the improved algorithm optimized BP neural network. *The International Journal of Advanced Manufacturing Technology* 2019; 105(1–4): 1497–1505, <https://doi.org/10.1007/s00170-019-04375-w>.
  12. Li HZ, Yang ZJ, Xu BB, Chen CH, Kan YN, Liu GF. Reliability Evaluation of NC Machine Tools considering Working Conditions. *Mathematical Problems in Engineering* 2016; 2016: 1–11, <https://doi.org/10.1155/2016/9842607>.
  13. Li YF, Zhang YJ, Zhao YQ, Shi XJ. Thermal-mechanical coupling calculation method for deformation error of motorized spindle of machine tool. *Engineering Failure Analysis* 2021; 128: 105597, <https://doi.org/10.1016/j.engfailanal.2021.105597>.
  14. Liu K, Sun MJ, Zhu TJ, Wu YL, Liu Y. Modeling and compensation for spindle's radial thermal drift error on a vertical machining center. *International Journal of Machine Tools and Manufacture* 2016; 105: 58–67, <https://doi.org/10.1016/j.ijmactools.2016.03.006>.
  15. Liu K, Wu JK, Liu HB, Sun MJ, Wang YQ. Reliability analysis of thermal error model based on DBN and Monte Carlo method. *Mechanical Systems and Signal Processing* 2021; 146: 107020, <https://doi.org/10.1016/j.ymsp.2020.107020>.
  16. Liu T. Thermal error modeling and active control method of electric spindle unit. Tianjin: Tianjin University 2016.
  17. Luo X, Xie FG, Liu XJ, Li J. Error modeling and sensitivity analysis of a novel 5-degree-of-freedom parallel kinematic machine tool. *Proceedings of the Institution of Mechanical Engineers, Part B: Journal of Engineering Manufacture* 2019; 233(6): 1637–1652, <https://doi.org/10.1177/0954405418782283>.
  18. Ma C, Yang J, Zhao L, Mei XS, Shi, H. Simulation and experimental study on the thermally induced deformations of high-speed spindle system. *Applied Thermal Engineering* 2015; 86: 251–268, <https://doi.org/10.1016/j.applthermaleng.2015.04.064>.
  19. Mohamed R, Fethi S, Abdelmadjid C. Study and Modeling of Machining Errors on the NC Machine Tool. *International Journal of Mechanical Engineering and Robotics Research* 2017; 6(1): 54–57, <https://doi.org/10.18178/ijmerr.6.1.54-57>.
  20. Shi H, Jiang CP, Yan ZZ, Tao T, Mei XS. Bayesian neural network-based thermal error modeling of feed drive system of CNC machine tool. *International Journal of Advanced Manufacturing Technology* 2020; 108(9–10): 3031–3044, <https://doi.org/10.1007/s00170-020-05541-1>.
  21. Srivastava AK, Veldhuis SC, Elbestawit MA. Modelling geometric and thermal errors in a five-axis CNC machine tool. *International Journal of Machine Tools and Manufacture* 1995; 35(9): 1321–1337, [https://doi.org/10.1016/0890-6955\(94\)00048-O](https://doi.org/10.1016/0890-6955(94)00048-O).
  22. Uhlmann E, Hu J. Thermal Modelling of a High-Speed Motor Spindle. *Procedia CIRP* 2012; 1(1): 313–318, <https://doi.org/10.1016/j.procir.2012.04.056>.
  23. Wang ZM, Yuan H. Enhancing machining accuracy reliability of multi-axis CNC machine tools using an advanced importance sampling method. *Eksplotacja i Niezawodność - Maintenance and Reliability* 2021; 23(3): 559–568, <https://doi.org/10.17531/ein.2021.3.17>.
  24. Xiang ST, Yao XD, Du ZC, Yang JG. Dynamic linearization modeling approach for spindle thermal errors of machine tools. *Mechatronics* 2018; 53: 215–228, <https://doi.org/10.1016/j.mechatronics.2018.06.018>.
  25. Yang AS, Yu XH, Zhuang JR, Lee CY, Hsieh WH. DOE-FEM based design improvement to minimize thermal errors of a high-speed spindle system. *Thermal Science and Engineering Progress* 2018; 8: 525–536, <https://doi.org/10.1016/j.tsep.2018.10.011>.
  26. Zhang ZL, Cai LG, Cheng Q, Lui ZF, Gu PH. A geometric error budget method to improve machining accuracy reliability of multi-axis machine tools. *Journal of Intelligent Manufacturing* 2019; 30(2): 495–519, <https://doi.org/10.1007/s10845-016-1260-8>.
  27. Zhang ZL, Cheng Q, Qi BB, Tao ZQ. A general approach for the machining quality evaluation of S-shaped specimen based on POS-SQP algorithm and Monte Carlo method. *Journal of Manufacturing Systems*, 2021, 60: 553–568, <https://doi.org/10.1016/j.jmsy.2021.07.020>.
  28. Zhang ZL, Qi Y, Cheng Q, Liu ZF, Tao ZQ, Cai LG. Machining accuracy reliability during the peripheral milling process of thin-walled components. *Robotics and Computer-Integrated Manufacturing* 2019; 59: 222–234, <https://doi.org/10.1016/j.rcim.2019.04.002>.
  29. Zhang ZS. Mechanism research of the contact thermal resistance and its application in thermal analysis of motorized spindles. Beijing: Beijing University of Technology 2018.
  30. Zhao CL, Guan XS. Thermal Analysis and Experimental Study on the Spindle of the High-Speed Machining Center. *AASRI Procedia* 2012; 1: 207–212, <https://doi.org/10.1016/j.aasri.2012.06.032>.
  31. Zhao HT, Yang JG, Shen JH. Simulation of thermal behavior of a CNC machine tool spindle. *International Journal of Machine Tools and Manufacture* 2007; 47(6): 1003–1010, <https://doi.org/10.1016/j.ijmactools.2006.06.018>.
  32. Zhao Y, Lin TM, Tang XQ. Geometric Error Modeling of Machine Tools Based on Screw Theory. *Procedia Engineering* 2011; 24: 845–849, <https://doi.org/10.1016/j.proeng.2011.11.2748>.
  33. Zheng DX, Chen WF. Effect of structure and assembly constraints on temperature of high-speed angular contact ball bearings with thermal network method. *Mechanical Systems and Signal Processing* 2020; 145: 106929, <https://doi.org/10.1016/j.ymsp.2020.106929>.
  34. Zhu SW, Ding GF, Qin SF, Lei J, Zhuang L, Yan KY. Integrated geometric error modeling, identification and compensation of CNC machine tools. *International Journal of Machine Tools and Manufacture* 2012; 52(1): 24–29, <https://doi.org/10.1016/j.ijmactools.2011.08.011>.